Quantitative experimental and numerical investigation of a vortex ring impinging on a wall

Drazen Fabris and Dorian Liepmann[a)]
Department of Mechanical Engineering, University of California, Berkeley, California 94720

Daniel Marcus
Lawrence Livermore National Laboratory, Livermore, California 94550

(Received 20 September 1995; accepted 12 April 1996)

A joint experimental and computational methodology is developed and applied to investigate a vortex ring impinging normally on a wall. The method uses digital particle image velocimetry to make planar flow measurements, which are then used to initialize a second-order finite difference calculation. The experiment and the simulation are compared at later times and agree extremely well. The ring undergoes two rebounds from the wall and continues to expand. During the approach to the wall, peak vorticity grows by 50% due to vortex stretching. Peak vorticity strengths of the secondary and tertiary vortices formed from the shedding boundary layer are 40% and 20% of the primary. In addition, a ring with a Gaussian core is simulated and compared to demonstrate the benefits of using realistic initial conditions. © *1996 American Institute of Physics.* [S1070-6631(96)01609-1]

I. INTRODUCTION

Recent improvements in experimental and numerical methods open up the possibility of combined investigations, which will substantially increase our understanding of complex fluid flows. Specifically, the development of digital particle image velocimetry (DPIV)[1,2] enables accurate experimental measurements of two-dimensional instantaneous velocity fields, whereas previous efforts are limited to flow visualization or ensembles of single-point measurements. These measurements can be integrated with simulations to provide both a validation of the evolution of the simulation and, more significantly, a physically realistic initialization. The validated numerical simulation can then confidently probe the fluid dynamics on a finer spatial and temporal scale than possible experimentally. In the following paper, we develop a methodology for combining experimental and numerical methods to quantitatively investigate the normal impingement of a vortex ring with a wall. The experimental measurements are compared with two simulations: one with realistic initial conditions and another, to demonstrate the importance of initial conditions, with simplifying assumptions.

A vortex ring impingement with a wall is a fundamental flow, which exhibits viscous and inviscid interactions. A vortex–surface interaction was first studied by Harvey and Perry;[3] a vortex ring–solid wall was studied by Walker *et al.*[4] and simulated by Shariff *et al.*,[5] Orlandi and Verzicco,[6] Liepmann *et al.*,[7] and Chu *et al.*[8] Similar investigations also include two rings interacting or a ring–free surface interaction.[9–13] Most of the experimental studies rely on dye visualizations or point measurements (LDV or hot wire); however, the dye experiments can, at best, provide qualitative estimates due to differing dye and vorticity diffusion rates while point measurements rely on the repeatability of the flow. Simulations, on the other hand, approach the flow with idealized assumptions, which hope to bracket the true flow conditions.[13] Using DPIV one can, in a few realizations, get a picture of the flow and then simulate the physics related to that specific experimental run.

The ring–wall interaction exhibits four primary stages of development: (1) vortex stretching as the ring approaches the wall; (2) viscous boundary layer growth; (3) instability in the boundary layer and separation; and (4) coalescence of the separated boundary layer into a ring of opposite signed vorticity (secondary ring). Further dynamics of the flow include an inviscid and viscous interaction between the opposite signed vortices, a repeat of the boundary layer shedding forming a tertiary ring, and instability of the secondary vortex. Extended descriptions of the phenomena were originally proposed by Walker *et al.*[4] and Orlandi and Verzicco.[6]

The process of vortex ring formation and translation is well described,[14–16] but an accurate two-dimensional (2-D) characterization of the core vortex distribution is uncertain. Theoretically many different distributions are proposed with interest in determining advection velocity or stability.[16–21] A fundamental assumption in most theoretical models is a ring with a small core diameter relative to the ring diameter, and a circular and symmetric distribution of vorticity in the core. Numerically, a variety of distributions are modeled[6,13,22] from a Kelvin–Hicks ring (core in full body rotation) to a Hill's vortex (thick diffuse ring). In addition, vortex generation methods in experiments vary without consistent comparisons of velocity or vorticity fields.[14,21,23,24] Therefore in order to accurately describe and simulate a vortex ring, the question of the distribution of the core vorticity needs to be resolved. The effect of core distribution should be especially important in the interaction with a wall. Cores with the same circulation (Reynolds number$=\Gamma/\nu$) but different strength of peak vorticity and distributions will lead to different strengths in the boundary layer flow and hence to secondary rings with different circulations and strengths.

[a)]Corresponding author. Phone: (510) 642-9360; fax: (510) 642-6163; Electronic mail: liepmann@euler.berkeley.edu

 1070-6631/96/8(10)/2640/10/$10.00 © 1996 American Institute of Physics

Downloaded¬05¬Mar¬2003¬to¬128.32.213.113.¬Redistribution¬subject¬to¬AIP¬license¬or¬copyright,¬see¬http://ojps.aip.org/phf/phfcr.jsp

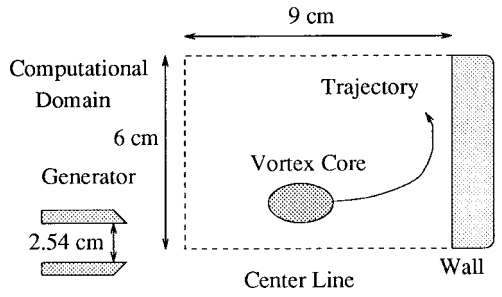

FIG. 1. Experimental configuration.

II. EXPERIMENTAL AND NUMERICAL METHOD

The general approach is to apply DPIV to measure the two-dimensional velocity field in a plane through the center of a laminar vortex ring. From the velocity field we compute vorticity that is used to initialize the simulation. The flow is simulated with a finite-difference projection method, which resolves the boundary layer and the secondary vortex roll-up, with greater detail than experimentally possible. The experiment and simulation are then compared at later times for mutual verification.

Figure 1 shows a schematic of the experiment. The diameter of the generating tube is 2.54 cm. The ring is generated several (4) diameters from the wall to allow formation transients to die out.[14] Two-dimensional velocities are measured in a planar $(r-x)$ cut with a DPIV method developed by Willert and Gharib.[1] The Reynolds number is chosen to be 1000 to ensure a two-dimensional vortex ring that is verified through flow visualization. The seed particles are fluorescein embedded polystyrene spheres of 80 μm diam and are illuminated with a Spectra-Physics 5 W argon-ion LASER light sheet. The video images are recorded with a CID Tech camera onto a real-time disk and digitized with a Vicom image processor. For improved spatial resolution, the field of view focuses on only half of the ring. Thirty velocity fields are generated per second of flow time with 799 realizations overall. Table I lists the experimental parameters. The velocity at points in the field of view but beyond the wall (as identified from an image) is manually set to zero. These are measurements due to image reflections off the wall. As a result, two columns of data are removed. Beyond this no vectors in the field were rejected or replaced by neighboring vectors. Willert and Gharib[1] estimate measurement uncertainty of 0.05 pixels (standard deviation) or one to two percent of the peak velocity.

TABLE I. Experimental parameters.

Generation parameters	Diameter	2.54 cm
	Maximum stroke	2.18 cm
	Reynolds number	1000 $(1/\nu)$
Measurement parameters	Field of view	6.8 cm×6.8 cm
	Digitized resolution	512×512
	Correlation window size	32×32
	Overlap	75%
	Vector resolution	61×61
	Vector spacing	1.1 mm
	LASER sheet thickness	3 mm

The computations implement a second-order projection method for the incompressible, axisymmetric Navier–Stokes equations,

$$\nabla \cdot u = 0, \tag{1}$$

$$\frac{\partial u}{\partial t} + u \cdot \nabla u = \nu\, \Delta u - \frac{1}{\rho}\, \nabla P, \tag{2}$$

developed by Bell, Colella, and Glaz.[25,26] The method incorporates a variant of the unsplit second-order Godunov methodology developed by Colella[27] for inviscid, compressible flows for the evaluation of the nonlinear advection terms in the momentum equations. This provides a temporal discretization that is second order for smooth flows and stable in regions with steep gradients, even for singular initial data and in the limit of vanishing viscosity. These properties make the method extremely well suited for flows that are characterized by fine structure and a wide range of length scales.

The method essentially decouples into three steps, an extrapolation of advective terms to a half time step,

$$(u \cdot \nabla u)^{n+1/2} = G(u^n), \tag{3}$$

a Crank–Nicholson viscous solve for the velocity at the next time,

$$\left(1 - \frac{\alpha}{2\,\Delta t}\,\Delta\right) u^* = u^n - \Delta t * \left((u \cdot \nabla u)^{n+1/2} - \frac{\alpha}{2}\,\Delta u^n\right), \tag{4}$$

and a projection to enforce continuity,

$$u^{n+1} = P(u^*). \tag{5}$$

Advection is calculated by a Godunov method using upwinding of variables where appropriate. The incompressible condition is satisfied through a discrete projection based on a Hodge decomposition first formulated by Chorin[28] and extended to second order by Bell *et al.*[26] The pressure field lies on a staggered grid from the velocity with the same node spacing and a preconditioned conjugate gradient solver is used for the projection and heat solves. The solver allows for grid domains that are not powers of two, which is more convenient for advecting rings. The Godunov method incorporates local slope limiters that keep the solution stable in regions of strong flow variations, including those due to strong local pressure gradients at the point of flow separation from the boundary.[25] The accuracy of the method is then governed by convergence of the solution with grid refinement with the time step determined by a Courant–Friedrichs–Lewy condition.

The objective is to make a velocity field measurement of a specific experimental run and with that measurement as an initialization closely match simulations to that particular flow case. The goal is then to use one or a limited number of DPIV measurements over a finite time to characterize the flow, but to avoid misrepresentations arising from experimental error. An outline of the procedure follows. We

Downloaded¬05¬Mar¬2003¬to¬128.32.213.113.¬Redistribution¬subject¬to¬AIP¬license¬or¬copyright,¬see¬http://ojps.aip.org/phf/phfcr.jsp

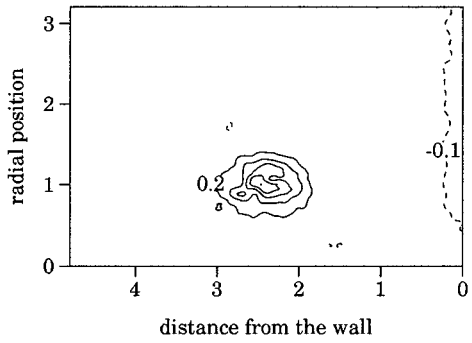

FIG. 2. Initial vorticity field. Positive contours every 0.2 and negative at −0.1. (Lengths are nondimensionalized with initial ring radius and vorticity with initial peak vorticity.)

choose to initialize from the vorticity field due to compact support (finite nonzero domain). The initial conditions are taken at a point where the ring formation process has been completed, and the ring is in translation. Seven consecutive realizations taken at $\frac{1}{30}$ of a second spacing are averaged to minimize the effects of noise and instantaneous structure of the ring. The frames chosen to be averaged are translated by the ring advection distance to match the positions of the cores and to avoid spreading of the vorticity field. Since the computation enforced axial symmetry it is only necessary to measure half the ring. Therefore, to improve the resolution, the measurement field contains half of the vortex ring plus a small area past the centerline of the ring, but it is vital to identify the position of the centerline. This is done by measuring the circulation of the viewed core with a square path line integral. The segment of the path that lies along the centerline is marched normal to the centerline. The position of this path segment that leads to the maximum circulation is identified as the centerline. Several positions from different time realizations are averaged to give the final position.

As a comparison, circulation can also be estimated from the advective speed relation, as done by Walker *et al.*[4]

$$U=\frac{\Gamma}{4\pi R}\left(\log\frac{8R}{a}-\frac{1}{4}\right). \tag{6}$$

Using the measured core radius (Fig. 3) and U determined from the trajectory of the centroid of vorticity [Fig. 6(c)], we find that the circulation is underestimated by 10% by this method.

The vorticity field used to initialize the simulation is shown in Fig. 2. The noncircular shape of the vortex ring is evident. It can also be seen that the ring has a relatively thick core. In addition, a natural convection boundary layer existed experimentally, which is shown drawing the fluid up at the edge. For the simulation, the boundary layer is left in the initialization. The computational method is not considered to be sensitive to the smoothness and continuity of the initialization field. High-frequency noise in the field will damp on its own and the projection in the code would immediately enforce continuity.

In order to show the importance of the initial condition on the performance of the numerical simulation, a ring with an initial condition of a core with a simple circular Gaussian distribution of vorticity is simulated. A Gaussian ring is often chosen for simulations to represent an inviscid ring. The Gaussian distribution has two free parameters that are set to match the flow. From physical reasoning, we choose to match Reynolds number (Γ/ν) and kinetic energy of the flow. The kinetic energy is of interest since it should determine the longevity of the vortex structures, and circulation should control the vortex dynamics during the impingement with the wall. In previous work,[4] physical quantities such as kinetic energy and impulse could not be measured and a comparison with simulations could not be made. Table II presents the measured quantities and their values for a ring with a Gaussian vortex core. For each row we match Reynolds number and another quantity and show the corresponding values for the unmatched quantities. In trying to match the impulse (case 3) the Gaussian core radius grew to a size beyond the ring radius. As a result the value of the impulse always remained below the experimental value and started to decline with further increase of the core radius. The Gaussian described in case 1 is subsequently used in the simulation.

The simulations are evolved on a 200 by 300 grid (6 cm by 9 cm) for 8 s of flow time and then the domain is redrawn to a 300 by 150 grid to prevent artificial boundary influences. The simulation is run on a CRAY 2. The simulation employed free-slip boundary conditions at the centerline and viscous no-slip conditions at the other boundaries. A small jump in some quantities, such as centroids, occurs when the flow is projected onto the new domain. To determine if the computation is fully resolved, the case presented is compared to lower and higher resolution cases, which were run for short periods of time. The highest resolution case agreed closely with the case presented, but was discontinued considering the computational cost. In addition, a simulated case is run with the initial data passed through a smoothing filter. The smoothed run shows no significant departure in the trajectory of the ring during the approach but a slightly lower

TABLE II. Possible cases for Gaussian matching. The Gaussian is matched to two global quantities. The Reynolds number (Γ/ν) is always matched.

	Gamma cm^2/s	Peak vorticity s^{-1}	Width (squared) cm^2	Kinetic energy erg	Impulse dyn/s	Enstrophy s^{-2}
Experiment	10.89	7.26	N/A	94.68	255.6	32.53
Case 1	10.89	4.771	0.7278	94.68	275.8	26.01
Case 2	10.89	7.26	0.4778	112.5	283.3	39.57
Case 3	10.89		could not match		255.6	

Downloaded¬05¬Mar¬2003¬to¬128.32.213.113.¬Redistribution¬subject¬to¬AIP¬license¬or¬copyright,¬see¬http://ojps.aip.org/phf/phfcr.jsp

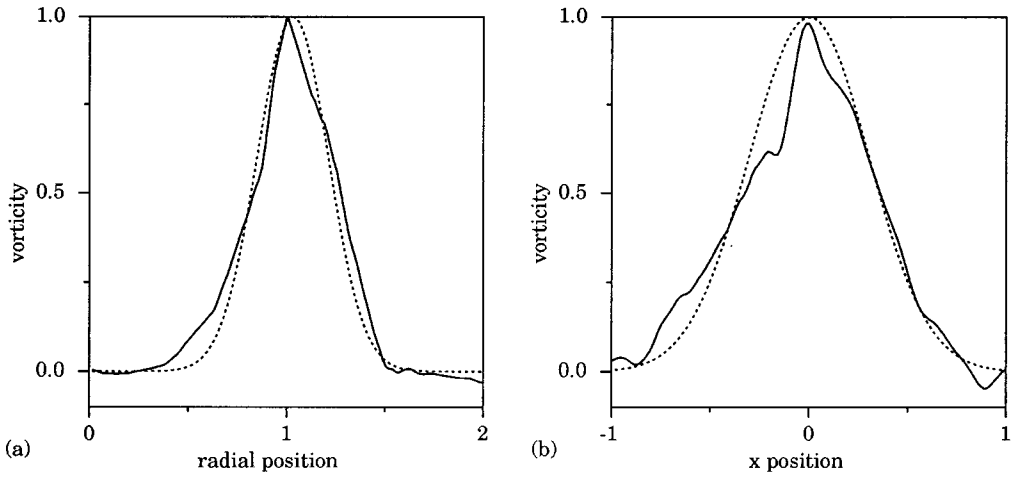

FIG. 3. Vorticity profiles from radial and x cuts through the center of the core of the initial distribution. Gaussian fits in dotted lines.

value of the peak vorticity and is not continued for this reason.

For quantitative comparisons, integral information from the experiment, kinetic energy and enstrophy, is interpolated and tabulated on spatial grids, with the same resolution as the computation. All quantities are nondimensionalized using R_0^2/Γ_0 for time and R_0 (initial radius) for length, and vorticity, circulation and kinetic energy are normalized with their initial values. The data are not filtered or smoothed in order to avoid imposing any preconceptions on the data. The high-frequency variations in the data, attributed to measurement noise, do not affect the global measurements. As a result the experimental measurements appear more irregular.

III. RESULTS

Through DPIV measurements we are able to identify and characterize the vorticity distribution of the ring and follow the interaction with the wall closely. The initial vorticity field shows that the ring is very thick with a large core radius relative to the ring radius, and that the core shape is not circular, but oblong and slightly weighted toward its centerline (Fig. 2). The front stagnation point and the rear stagnation point are different in shape, which shows the lack of reflective symmetry in the core. To compare with earlier LDV measurements, cross sections of the vorticity are taken through the core, both normal and parallel to the translation direction (Fig. 3). The distributions show Gaussian characteristics with different broadening widths of 0.254 for the radial distribution and 0.426 for the x distribution. These profiles compare well with other experimental measurements (DPIV and LDV),[20] but in comparison to Fig. 2 the vorticity field obviously has a more complex structure to its shape than seen in the cross-sectional profiles.

The vortex–wall interaction is shown in Fig. 4. The growth of the boundary layer, separation, and interaction is seen in Figs. 4(b)–4(d). The relative strengths, positions, and general shapes of the structures are consistent from one measurement to the next, while the high frequencies are an artifact of the experimental noise. Vortex stretching is evident through a decrease in the primary vortex cross-sectional area and an increase in the peak vorticity by 50% during time $t=10$–17 [Figs. 4(a)–4(c)]. As the ring approaches the wall the strength of the boundary layer increases dramatically up to a peak vorticity of -1.3 [Fig. 4(b)]. In addition, at $r=2.2$, negative vorticity separates from the boundary layer to form the secondary ring. In forming the secondary vortex and in the further vortex interactions, the primary ring becomes distorted [Figs. 4(b) and 4(c)]. In comparison, the secondary vortex is more distorted and stretched as it rotates around the primary. As the flow develops, the strength of the peak vorticity of the secondary vortex is 0.4 ± 0.04 of that of the primary. Finally, a repeat of the shedding process forming the tertiary ring can be seen in Fig. 4(d). The tertiary vortex has a peak vorticity strength of 0.2 of the primary vortex.

The simulation shows the same process in Fig. 5, but with greater detail in the boundary layer. The general shapes and positions and strengths of the vortices are very similar to the experiment, including the characterization of the secondary vortex. We see that the secondary vortex is the termination and coalescence of a shear layer that is being pulled away from the boundary layer [Fig. 5(c)]. The final separation of the secondary vortex from the shear layer occurs through diffusive cancellation of vorticity between the shear layer and the primary vortex [Fig. 5(d)]. Note that the high-frequency variations in the initial conditions are smoothed out by the simulation. This effect is due to both the two-dimensional simulation not allowing any three-dimensional structures to exist and viscous damping of high-frequency experimental noise.

To compare the simulation to the experiment quantitatively we look for a reduced characterization of the vortex dynamics in the trajectories of the primary and secondary vortices. These are shown for the experiment and the computations in Figs. 6(a) and 6(b). The positions of the primary and secondary rings are determined by the positions of the local extrema of the vorticity. Due to high noise in the peak value and position, the experimental trajectory of the peak of vorticity is curve fit with a seventh-order polynomial. Figure

Downloaded¬05¬Mar¬2003¬to¬128.32.213.113.¬Redistribution¬subject¬to¬AIP¬license¬or¬copyright,¬see¬http://ojps.aip.org/phf/phfcr.jsp

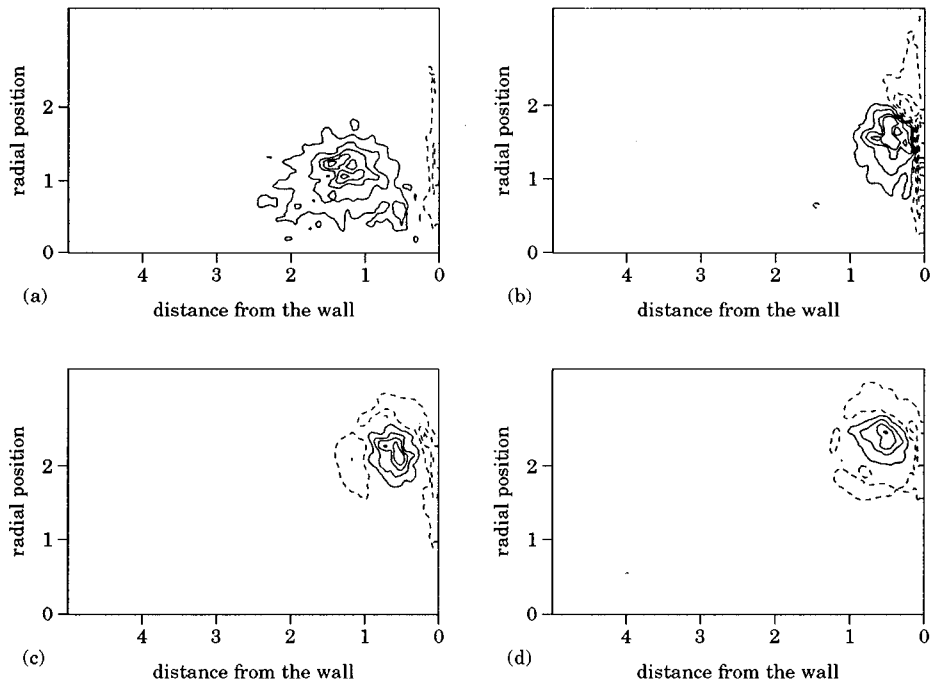

FIG. 4. Experimental vorticity contours at (a) $t=5.88$, (b) $t=11.77$, (c) $t=23.54$, and (d) $t=29.43$. Contours at 0.5 ± 1.5 with negative contours dashed.

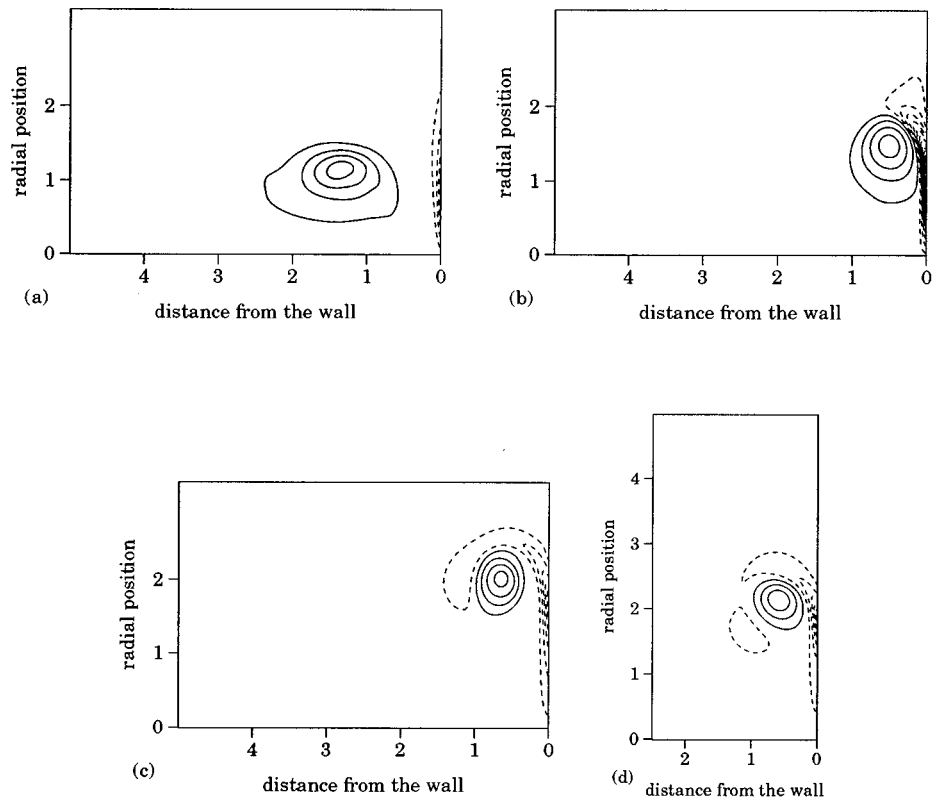

FIG. 5. Contour plots of the simulation at the same times.

Downloaded¬05¬Mar¬2003¬to¬128.32.213.113.¬Redistribution¬subject¬to¬AIP¬license¬or¬copyright,¬see¬http://ojps.aip.org/phf/phfcr.jsp

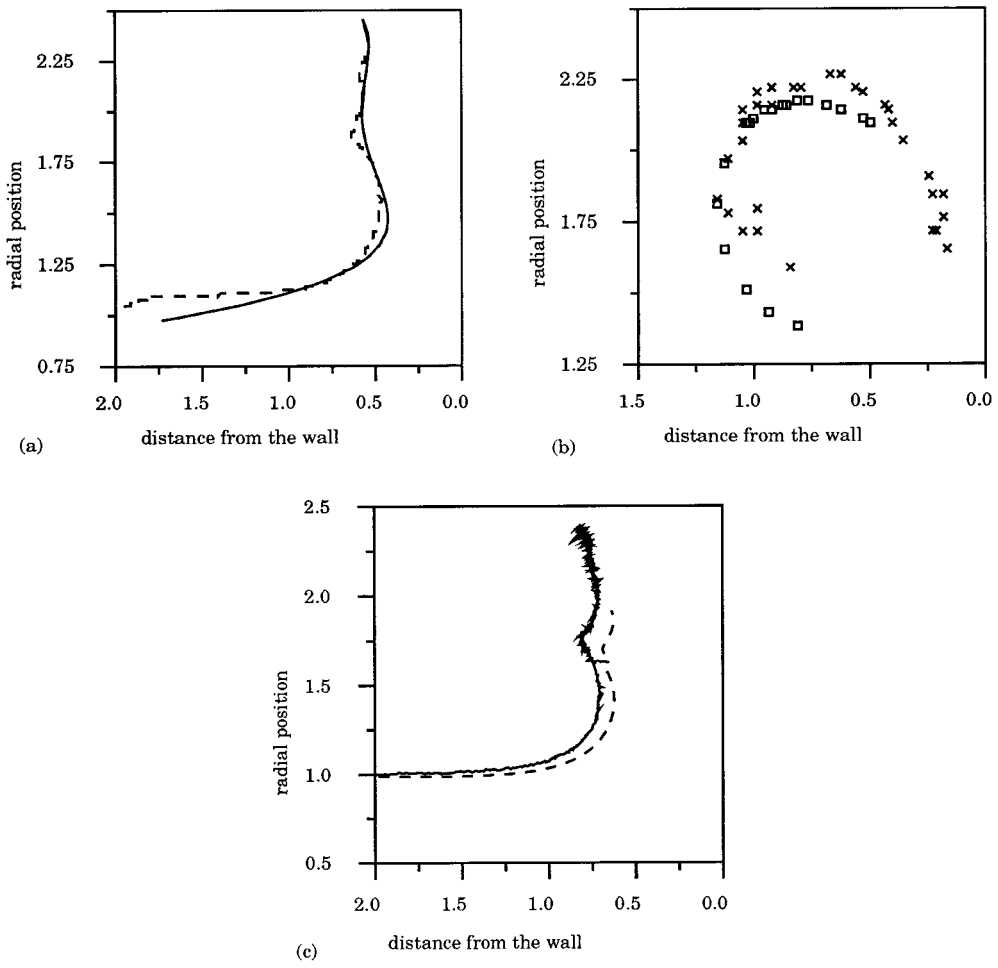

FIG. 6. Trajectories of primary and secondary vortices: (a) trajectory of peak of positive vorticity, (b) positions of the peak of the secondary vortex, and (c) trajectory of the centroid of positive vorticity. The experiment is shown in solid lines and x's. The simulation is shown in dashed lines and boxes.

6(c) shows the centroid of positive vorticity. The centroid provides an integral measurement of the position of ring and shows some of the dynamics of the flow, but is biased away from the position of the peak of vorticity due to experimental noise in the farfield.

The trajectory of peak vorticity, Fig. 6(a), shows that the actual positions of the experimental and numerical rings agree very well. The straight approach toward the wall shown in Fig. 6(c) compares well with Walker *et al.*[4] The experiment shows at least a single rebound in both centroid and peak of vorticity [Figs. 6(c) and 6(a)], while the simulation shows both a primary and secondary rebound more distinctly at $t=22.0$, $r=1.91$ and $t=42$, $r=2.2$ in the peak of vorticity. The ring continues to expand at this Reynolds number, which agrees with earlier studies.[10] In addition, the secondary vortex ring in both cases follows the same path. In the simulation the genesis of the secondary vortex is identified, where the separating boundary layer develops a local minimum. Experimentally the secondary vortex appears earlier, but, considering noise and resolution, the exact point of formation is difficult to judge.

A comparison of global quantities, such as circulation history, provides a good consistency check for the simulation. Figure 7 shows the positive circulation (in the ring), negative circulation (in the boundary layer), and total circulation. Circulation is calculated by summing the vorticity of the appropriate sign over the entire field. Again, the simulation can be seen to undergo a transient stage ($t=0$–4), where the high-frequency variations in vorticity cancel. These

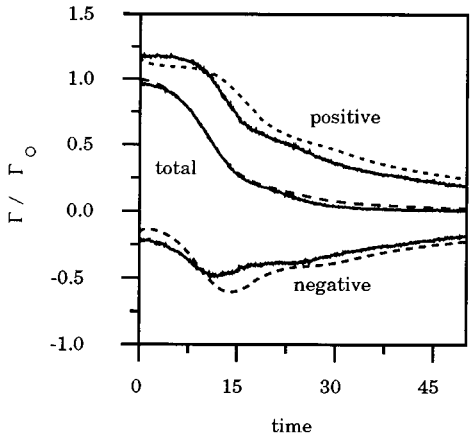

FIG. 7. Positive, negative, and total circulation.

Downloaded¬05¬Mar¬2003¬to¬128.32.213.113.¬Redistribution¬subject¬to¬AIP¬license¬or¬copyright,¬see¬http://ojps.aip.org/phf/phfcr.jsp

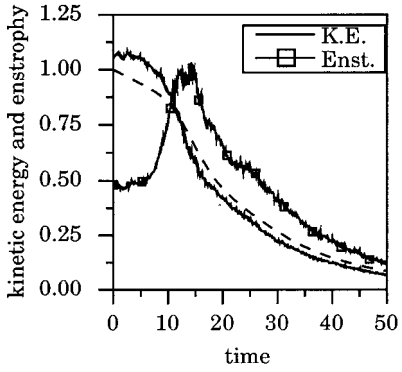

FIG. 8. Kinetic energy and enstrophy. The enstrophy is shown with the boxes.

variations occur both in the vortex ring and in the farfield. At later times we expect the experimental measurements to undervalue the circulation due to difficulties in resolving the fine structure of the boundary layer. Looking at the negative circulation one can see strong boundary layer growth from $t=6$–12 with shedding of vorticity from the boundary layer indicated here at the minimum of the negative circulation. The highest rate of decay of total circulation occurs early, $t=6$–14, while there is strong development of the boundary layer. After this point the strong vortex layer rolls up into the secondary ring and diffuses with the primary ring. A repeat of this process with the formation of the tertiary ring is seen at $t=24$–36.

Figure 8 shows the kinetic energy and enstrophy. The kinetic energy decay prior to the interaction with the wall ($t=0$–8) shows a large viscous effect that supports the thick ring characterization with diffusion during the advection process. The dissipation greatly increases as the ring interacts with the wall. The experimental measurements of enstrophy show significant boundary layer vorticity production from $t=10$–15 and 22–26 and compare well with previous computations.[8]

Figure 9 shows maximum and minimum vorticity. Both the experiment and the simulation show an increase in the vortex strength due to stretching from $t=9$–15. At the same time the boundary layer grows to its maximum vorticity, which peaks and starts to decay just before the peak of positive vorticity due to stretching. This predication of decay of the peak vorticity in the boundary layer suggests a complex interaction that must depend on the distribution of vorticity as well as on its peak values. Diffusion of high-frequency variations during the initial transience in the simulation reduces the values of peak positive vorticity in the simulation compared to the experimental results. In addition, the DPIV measurements show a fluctuation in the peak vorticity, which is due to velocity biasing toward fluid velocities at the particle locations. DPIV measurements only track particle displacements and there are difficulties in correctly identifying fluid velocity variations (such as the exact position of the peak of vorticity) that are on a scale comparable to the particle separation or the interrogation zone size. For the same reason the vorticity strength in the boundary layer is overestimated due to the small scale of the layer relative to the positional approximation of measurement. Increasing computational grid refinement increased the strength of the maximum negative vorticity, which agrees with Orlandi.[6]

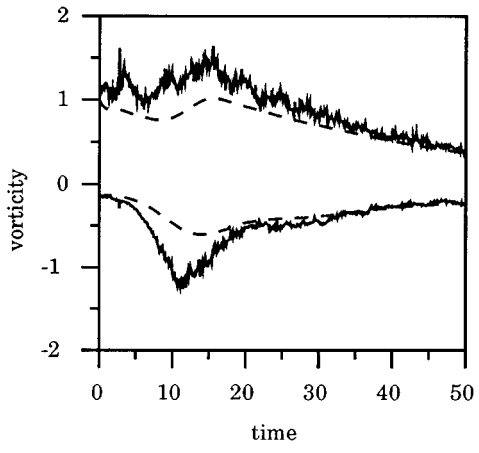

FIG. 9. Extrema of vorticity.

For a more global comparison we look at vorticity contours in between the secondary and tertiary vortex shedding (Fig. 10). In general, the simulation agrees extremely well with the experiment showing identical features and comparing quantitatively. The experiment showed a slightly higher negative vortex core and a slightly lower positive vortex core. This discrepancy is attributed to the negative vorticity of the preexisting natural convection layer being rolled up. The separation point of the boundary layer remains relatively fixed on the wall, and the primary ring sweeps negative vorticity from the wall past the separation point. In both images the circulation of the secondary ring is substantially weaker than that of the primary, but is strong enough to cause the primary ring to rebound through an inviscid interaction but not cause the primary ring to contract radially.

A comparison of the simulation with real initial conditions with the Gaussian case illustrates the advantage of using appropriate starting conditions. Figure 11 shows the interaction of the Gaussian core with the wall. The more diffuse core creates a stronger secondary vortex due to a longer time of interaction before the secondary vortex was shed. The comparison of the position of peak vorticity for the two simulations is shown in Fig. 12. The Gaussian initial condition is unstable due to its large and diffuse distribution and goes through a process of development as it approaches the wall. The same effect is reported in other numerical work.[5,6,13] The simulation with real initial conditions shows two rebounds with continued expansion while the Gaussian case expands further and then undergoes a loop. The primary ring contraction results from the overestimation of the secondary vortex circulation. This contraction is not seen at this Reynolds number in our experiment, but has been reported for higher Reynolds numbers.[4,6]

Figure 13 shows the effect of computational refinement. For comparison the motion of the centroid of vorticity is considered due to the smoothness of the experimental measurement for this quantity. The lower resolution simulation

Downloaded¬05¬Mar¬2003¬to¬128.32.213.113.¬Redistribution¬subject¬to¬AIP¬license¬or¬copyright,¬see¬http://ojps.aip.org/phf/phfcr.jsp

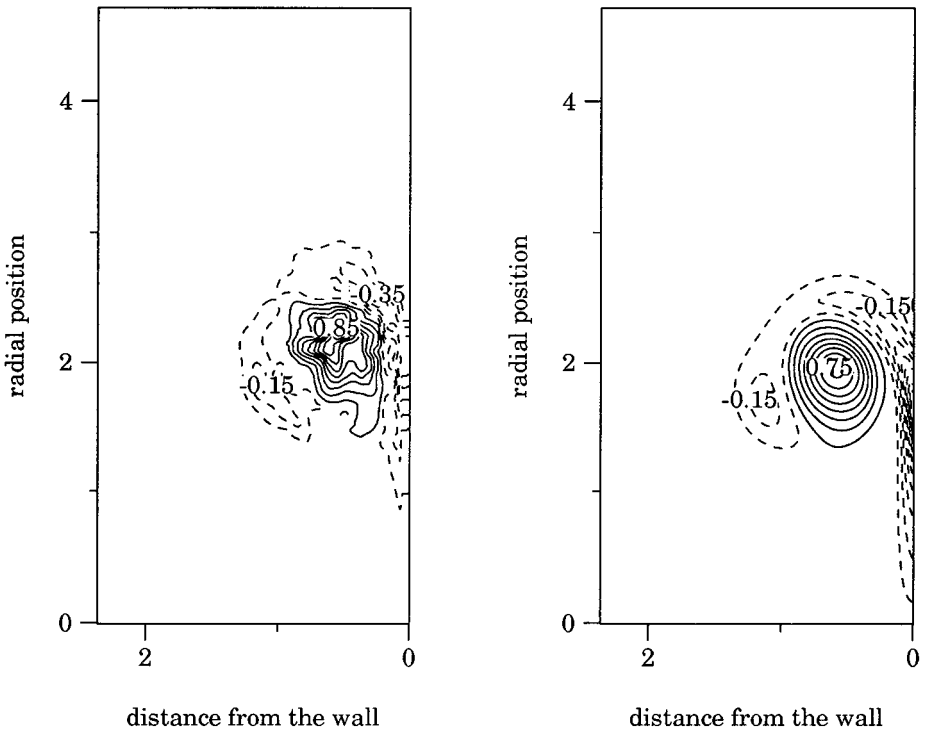

FIG. 10. Vorticity contours in the experiment and the simulation at $t=26.0$ (after the roll-up of the boundary layer into the secondary vortex and before the generation of the third).

expands radially farther than is realistic, which suggests that the boundary layer strength is to low due to under refinement. In the higher resolution simulation the radial positions of the rebound and closest approach to the wall agree well with the experiment, indicating that the simulation is sufficiently resolved. The highest resolution (400 by 600) agrees closely with the (200 by 300), but was not computed to this temporal extent due to computational cost.

IV. CONCLUSIONS

An overall methodology for combining modern experimental and numerical techniques is applied to a laminar vortex ring interaction normally with a wall. A DPIV system is

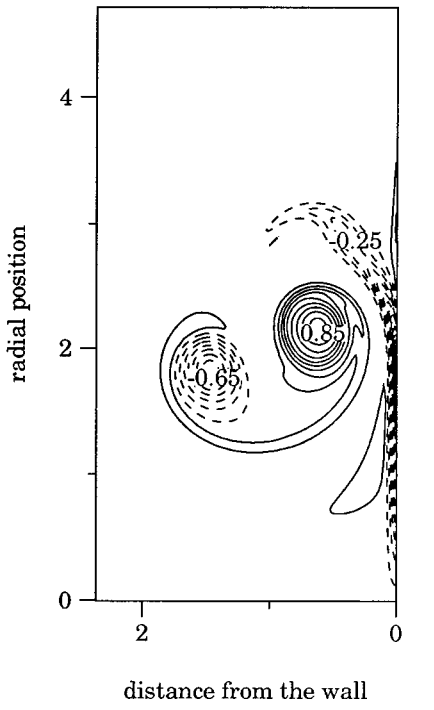

FIG. 11. Vorticity contours of the simulation with Gaussian initial conditions at the same point in time.

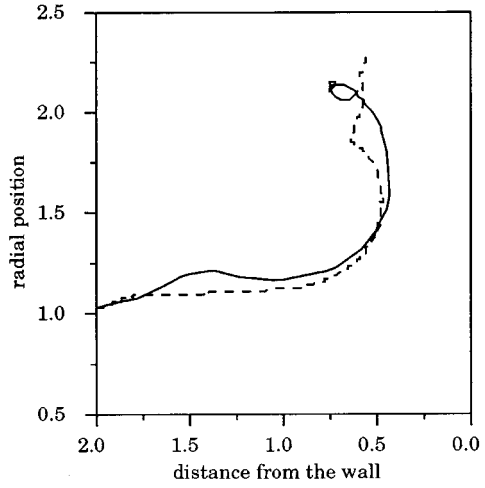

FIG. 12. Trajectories of the primary ring for the two simulated cases. The Gaussian case is shown solid and the case with real initial conditions is shown dotted.

Downloaded¬05¬Mar¬2003¬to¬128.32.213.113.¬Redistribution¬subject¬to¬AIP¬license¬or¬copyright,¬see¬http://ojps.aip.org/phf/phfcr.jsp

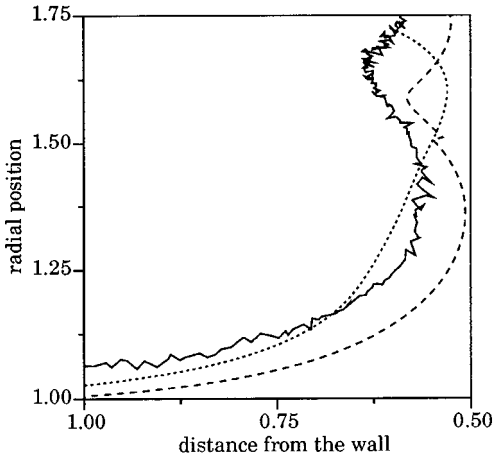

FIG. 13. Trajectory of the primary ring (centroid of vorticity). The experiment is shown solid, the high resolution (200×300) is shown dashed, and the low resolution (100×150) is shown dotted.

used to measure a physically accurate vorticity distribution in a vortex ring core. From this initial condition a numerical simulation is evolved that uncovers more details of the flow. Further DPIV measurements at later times and the simulation are quantitatively compared. To demonstrate the importance of a physically realistic initial condition, a ring with an assumed circular Gaussian core is simulated and compared.

In this study we present the first experimental velocity field measurements throughout the interaction of a vortex ring, Reynolds number=1000, with a solid wall. The boundary layer is seen to roll up into an opposite signed vortex whose circulation is sufficient to induce a rebound of the primary ring but substantially smaller than the primary. The primary vortex continues to expand and the boundary layer shedding process repeats with the formation of the tertiary ring. In addition, kinetic energy, enstrophy, circulation, and peak vorticity trends are measured and found to be consistent with a thick vortex ring, rapid boundary layer growth, and two shedding phases. Large rates of dissipation of circulation occur as the vortex initially interacts with the boundary and decrease after the boundary layer was shed. As evidence of vortex stretching, peak vorticity grows by 50% as the ring approached the wall.

A matching numerical simulation is evolved using experimental data as an initialization. From the greater detail available in the simulation the primary ring is identified to rebound twice from the wall. The first rebound is an inviscid interaction with the secondary vortex and the second rebound is an interaction with the tertiary.

To demonstrate the importance of a physically accurate initialization for computations, an initialization of a circular, Gaussian ring is simulated. Without an accurate measurement of physical quantities, such as kinetic energy and impulse, there exists uncertainty in choosing the Gaussian's width and strength. In all cases the Gaussian distribution mismatches the measured quantities by 10%–20%. The Gaussian case shows qualitatively and quantitatively different results. The peak vorticity in the secondary vortex is too high and the trajectory of the primary ring undergoes a contraction that is not seen in this experiment.

ACKNOWLEDGMENTS

The authors would like to thank for their contributions and advice: Alexander Weigand, Ömer Savaş, and Phillip Colella. Research at UC Berkeley was supported in part by the U.S. Department of Energy HPCCP Grant No. DE-FG03-92ER25140. The work of Dan Marcus was performed under the auspices of the U.S. Department of Energy by the Lawrence Livermore National Laboratory under Contract No. W-7405-Eng-48. Support under Contract No. W-7405-Eng-48 was provided by the DOE Office of Scientific Computing Applied Mathematical Sciences Program DOE HPCC Program.

[1] C. E. Willert and M. Gharib, ''Digital particle image velocimetry,'' Exp. Fluids **10**, 181 (1991).
[2] R. J. Adrian, ''Particle-imaging techniques for experimental fluid mechanics,'' Annu. Rev. Fluid Mech. **23**, 261 (1991).
[3] J. K. Harvey and F. J. Perry, ''Flowfield produced by trailing vortices in the vicinity of the ground,'' AIAA J. **9**, 1659 (1971).
[4] J. D. A. Walker, C. R. Smith, A. W. Cerra, and T. L. Dogilaski, ''The impact of a vortex ring on a wall,'' J. Fluid Mech. **181**, 99 (1987).
[5] K. Shariff, R. Verzicco, and P. Orlandi, ''A numerical study of three-dimensional vortex ring instabilities: Viscous corrections and early nonlinear stage,'' J. Fluid Mech. **279**, 351 (1994).
[6] P. Orlandi and R. Verzicco, ''Vortex rings impinging on walls: Axisymmetric and three-dimensional simulations,'' J. Fluid Mech. **256**, 615 (1993).
[7] D. Liepmann, D. Dommermuth, and A. Weigand, ''Quantitative experimental and numerical investigation of a vortex ring impinging on a wall,'' Bull. Am. Phys. Soc. **36**, 2320 (1991).
[8] C.-C. Chu, C.-T. Wang, and C.-C. Chang, ''A vortex impinging on a solid plane surface—Vortex structure and surface force,'' Phys. Fluids **7**, 1391 (1995).
[9] P. Schatzle, ''An experimental study of fusion of vortex rings,'' Ph.D. thesis, Grad. Aero. Labs., California Institute of Technology, 1987.
[10] T. T. Lim, T. B. Nichols, and M. S. Chong, ''A note on the cause of rebound in the head-on collision of a vortex ring with a wall,'' Exp. Fluids **12**, 41 (1991).
[11] D. L. Marcus and J. B. Bell, ''Numerical simulation of a viscous vortex ring interaction with a density interface,'' Phys. Fluids **6**, 1505 (1994).
[12] W. J. A. Dahm, C. M. Scheil, and G. Tryggvason, ''Dynamics of vortex interaction with a density interface,'' J. Fluid Mech. **205**, 1 (1989).
[13] S. Stanaway, K. Shariff, and F. Hussain, ''Head-on collision of viscous vortex rings,'' *Proceedings of the Summer Program*, Center for Turbulence Research, Stanford, CA, 1988, pp. 287–309.
[14] N. Didden, ''On the formation of vortex rings: Rolling-up and production of circulation,'' J. Appl. Math. Phys. (Z. Angew. Math. Phys.) **30**, 101 (1979).
[15] T. Maxworthy, ''The structure and stability of vortex rings,'' J. Fluid Mech. **51**, 15 (1972).
[16] P. G. Saffman, *Vortex Dynamics* (Cambridge University Press, Cambridge, 1992).
[17] Sir H. Lamb, *Hydrodynamics* (Cambridge University Press, Cambridge, 1993).
[18] J. Norbury, ''A family of steady vortex rings,'' J. Fluid Mech. **57**, 417 (1973).
[19] S. E. Widnall and J. P. Sullivan, ''On the stability of vortex rings,'' Proc. R. Soc. London Ser. A **332**, 335 (1973).
[20] A. Weigand, ''The response of a vortex ring to a transient, spatial cut,'' Ph.D. thesis, University of California, San Diego, CA, 1993.
[21] K. Shariff and A. Leonard, ''Vortex rings,'' Annu. Rev. Fluid Mech. **24**, 235 (1992).
[22] Q.-Y. Ye and C. K. Chu, ''Unsteady evolution of vortex rings,'' Phys. Fluids **7**, 795 (1995).
[23] D. I. Pullin, ''Vortex ring formation at tube and orifice openings,'' Phys. Fluids **22**, 401 (1979).

Downloaded¬05¬Mar¬2003¬to¬128.32.213.113.¬Redistribution¬subject¬to¬AIP¬license¬or¬copyright,¬see¬http://ojps.aip.org/phf/phfcr.jsp

[24]T. Maxworthy, ''Some experimental studies of vortex rings,'' J. Fluid Mech. **81**, 465 (1977).
[25]J. B. Bell and D. L. Marcus, ''A second-order projection method for variable-density flows,'' J. Comput. Phys. **101**, 334 (1992).
[26]J. B. Bell, P. Colella, and H. M. Glaz, ''A second-order projection method for the incompressible Navier–Stokes equations,'' J. Comput. Phys. **85**, 257 (1989).
[27]P. Colella, ''Multidimensional upwind methods for hyperbolic conservation laws,'' J. Comput. Phys. **87**, 171 (1990).
[28]A. J. Chorin, ''On the convergence of discrete approximations to the Navier–Stokes equations,'' Math. Comput. **23**, 341 (1969).

Downloaded¬05¬Mar¬2003¬to¬128.32.213.113.¬Redistribution¬subject¬to¬AIP¬license¬or¬copyright,¬see¬http://ojps.aip.org/phf/phfcr.jsp